Solar Site Survey for the Advanced Technology Solar Telecope. I. Analysis of the Seeing Data

H. Socas-Navarro

High Altitude Observatory, NCAR[1], 3450 Mitchell Lane, Boulder, CO 80307-3000, USA

`navarro@ucar.edu`

J. Beckers

University of Chicago, IL 60637, USA

P. Brandt

Kiepenheuer-Institut für Sonnerphysik, Schöneckstrasse 6, Freiburg, 79104, Germany

J. Briggs

National Solar Observatory, Sunspot, NM 88349, USA

T. Brown

High Altitude Observatory, NCAR, 3450 Mitchell Lane, Boulder, CO 80307-3000, USA

W. Brown

Atmospheric Technology Division, NCAR, 1850 Table Mesa Dr, Boulder, CO 80307-3000, USA

M. Collados

Instituto de Astrofísica de Canarias, Avda Vía Láctea s/n, E38200, La Laguna (Tenerife), Spain

C. Denker

New Jersey Institute of Technology, Dr. Martin Luther King Blvd., Newark, NJ 07102-1982, USA

S. Fletcher

National Solar Observatory, Sunspot, NM 88349, USA

S. Hegwer

National Solar Observatory, Sunspot, NM 88349, USA

F. Hill

National Solar Observatory, PO Box 26732, Tucson, AZ 85726-6732, USA

T. Horst

Atmospheric Technology Division, NCAR, 1850 Table Mesa Dr, Boulder, CO 80307-3000, USA

M. Komsa

National Solar Observatory, Sunspot, NM 88349, USA

J. Kuhn

University of Hawaii, Institute of Astronomy, 2680 Woodlawn Drive, Honolulu, HI 96822, USA

A. Lecinski

High Altitude Observatory, NCAR, 3450 Mitchell Lane, Boulder, CO 80307-3000, USA

H. Lin

University of Hawaii, Institute of Astronomy, 2680 Woodlawn Drive, Honolulu, HI 96822, USA

S. Oncley

Atmospheric Technology Division, NCAR, 1850 Table Mesa Dr, Boulder, CO 80307-3000, USA

M. Penn

National Solar Observatory, PO Box 26732, Tucson, AZ 85726-6732, USA

T. Rimmele

National Solar Observatory, Sunspot, NM 88349, USA

K. Streander

High Altitude Observatory, NCAR, 3450 Mitchell Lane, Boulder, CO 80307-3000, USA

ABSTRACT

The site survey for the Advanced Technology Solar Telescope concluded recently after more than two years of data gathering and analysis. Six locations, including lake, island and continental sites, were thoroughly probed for image quality and sky brightness. The present paper describes the analysis methodology employed to determine the height stratification of the atmospheric turbulence. This information is crucial because day-time seeing is often very different between the actual telescope aperture (~ 30 m) and the ground. Two independent inversion codes have been developed to analyze simultaneously data from a scintillometer array and a solar differential image monitor. We show here the results of applying them to a sample subset of data from May 2003, which was used for testing. Both codes retrieve a similar seeing stratification through the height range of interest. A quantitative comparison between our analysis procedure and actual *in situ* measurements confirms the validity of the inversions. The sample data presented in this paper reveal a qualitatively different behavior for the lake sites (dominated by high-altitude seeing) and the rest (dominated by near-ground turbulence).

Subject headings: atmospheric effects — methods: data analysis — site testing — telescopes

1. Introduction

The Advanced Technology Solar Telescope (ATST, Keil et al. 2003), with its 4-meter aperture, will be the largest solar telescope in the world. A suite of advanced instrumentation will allow for unprecedented resolution and precision imaging, spectroscopy and polarimetry at visible and infrared wavelengths. In order to address the most challenging problems in modern solar physics, ATST's highest priorities are oriented towards high-resolution and coronal science. Obviously, these are aspects in which the site selection will have a strong impact and therefore should be considered very carefully in the decision of the telescope location. The ATST Site Survey Working Group (SSWG) was created in 2000 with an open

---

call to the international community. Its goal was essentially to test the best solar observatories in the world and produce a recommendation to maximize the scientific capabilities of the ATST. More especifically, a set of quantitative goals were set for the ATST site:

- Clear time of 70%, or 3000 annual hours of sunshine.

- 1800 annual hours of seeing with a Fried parameter r_0 better than 7 cm, including at least 100 continuous 2-hour blocks.

- 200 annual hours of $r_0 > 12$ cm, including at least 10 continuous 2-hour blocks.

- Large isoplanatic angle for adequate performance of the adaptive optics system over a large field of view. This goal is equivalent to demanding minimal turbulence at high altitude.

- 480 annual hours with a sky brightness smaller than 25 millionths of the disk value at a distance of 1.1 solar radii. The radial profile curve should follow a power law with an exponent $R = 0.8$ or steeper. These conditions should be met in at least 40 continuous 4-hour block per year.

- 600 annual hours with precipitable water vapor below 5 mm, including at least 40 continuous 4-hour blocks.

Only two comparative studies of solar observatories had been conducted prior to this work. The JOSO organization studied nearly 40 sites in Europe to conclude that Observatorio del Teide in Tenerife (Canary Islands) provided the better conditions recorded in their data (Brandt & Woehl 1982; Brandt & Righini 1985). The other work is that of the Caltech survey, which considered 34 sites in the southern California area to locate what is now the Big Bear Solar Observatory (BBSO; Zirin & Mosher 1988).

Initially, a list of 72 well-established observatories and some promising undeveloped sites was compiled. Since the ATST SSWG had only sufficient resources for extensive testing of up to six sites, a first decision had to be made in the absence of any actual measurements. This decision was made based on previous observing experience of the group members. A first round of discussion quickly resulted in the selection of BBSO, La Palma (Canary Islands) and Sacramento Peak (New Mexico), which have an outstanding record in producing high-quality solar observations. The SSWG also selected Hawaii, and in particular Haleakala (on the island of Maui) was preferred over Mauna Loa and Mauna Kea after taking feasibility issues into account. Diverse other considerations later resulted in the choice of Panguitch Lake (Utah) and San Pedro Mártir (Mexico) for the final two slots.

The instrumentation deployed at the six candidate sites includes a scintillometer array (SHABAR) and a Solar Differential Image Motion Monitor (S-DIMM). Both instruments have been described in a recent paper by Beckers (2001). The SHABAR and S-DIMM are used to determine the atmospheric turbulence as a function of height. It must be noted that daytime seeing conditions are often strongly dependent on height above the ground. Thus, the ATST site survey needed to determine the observing conditions at the telescope aperture height, approximately 35 meters above the ground (the actual height is still to be decided). The site survey instrumentation was placed at a height of 8 meters (6-meter stand plus a 2-meter telescope pier), which is high enough to avoid the lower part of the surface boundary layer but not so high that wind jitter could become a significant problem.

Data from the SHABAR and S-DIMM instruments have been gathered and analyzed until August 2004. In October 2004, the ATST SSWG presented a final recommendation and produced an exhaustive document with a detailed report of the site survey process. The SSWG report is publicly available for download from the ATST website (http://atst.nso.edu/). That document contains abundant technical documentation and the reader is referred to it for further details. The present series of papers is a formal publication of the most relevant results. This first paper describes the inversion methods used to infer the atmospheric turbulence and the Fried parameter from the SHABAR/S-DIMM data. The methods have been extensively tested by means of simulations, comparison between different algorithms and also with *in situ* measurements. One month of data (May 2003) was used for testing and fine tuning the algorithms before being applied systematically to the entire site survey period.

2. Derivation of $C_n(h)$

2.1. Basic relations

The final objective is to determine the Fried parameter as a function of height, $r_0(h)$. This parameter depends not only on the turbulence at a height h but also everything above it. With some assumptions (see Hickson & Lanzetta 2004 for a complete derivation), r_0 can be obtained as:

$$r_0^{-5/3}(h) = C \sec(z) \int_h^\infty C_n^2(h)dh \,, \tag{1}$$

where C is a constant, z is the zenith angle and C_n^2 (which represents the amplitude of the refraction index fluctuations) characterizes the local atmospheric turbulence at height h. Notice that h denotes height above the instrument, which in our case is located 8 meters above the ground.

The covariances (B_I) of the brigthness fluctuations measured by two detectors, separated by a distance d in the SHABAR array, are related to C_n^2 by:

$$B_I(d) = 0.38 \int_0^\infty W(h,d)C_n^2(h)dh\,, \tag{2}$$

where the $W(h,d)$ are known functions with analytical expressions. If a is the detector diameter and α is twice the tangent of the solar radius (which we consider approximately constant though the year):

$$W(h,d) = \frac{32\pi h^2 \sec^3 z}{(a + \alpha h \sec z)^{7/3}} Q\left(\frac{d}{a + \alpha h \sec z}\right)\,,$$
$$Q(s) = \int_0^\infty [J_1(\pi f)]^2 J_0(2\pi f s) f^{-2/3} df\,, \tag{3}$$

with J_0 and J_1 being the Bessel functions. The total scintillation can be obtained from the expressions above as $B_I(d = 0)$. The kernels $W(h,d)$ are shown in Fig 1. It can be deduced from this figure that the B_I corresponding to further separations (larger values of d) have their sensitivity peak at higher atmospheric layers. Fig 2 shows average values of $B_I(d)$ measured at the six candidate sites. Not surprisingly, the covariances decrease with the detector separation d.

2.2. The inversion codes

The inversion strategy that we employed to solve for $C_n^2(h)$ in Eq (2) is a non-linear least-squares iterative fitting combined with singular-value decomposition (SVD) of the covariance matrix. The details of the implementation can be found, e.g. in Press et al. (1986), but the basic idea is the following. One starts with an initial guess for the $C_n^2(h_i)$ (where h_i are the gridpoints of the atmospheric discretization). With this initial model we calculate the 15 different covariances $B_I(d_{jk})$ (where d_{jk} is the separation between each pair of detectors j and k in the SHABAR instrument), the total scintillation $B_I(d = 0)$ and the Fried parameter at the base of the atmosphere $r_0(h = 0)$ (measured by the S-DIMM instrument), using Eqs (1) and (2). The derivatives of these parameters with respect to the $C_n^2(h)$ (the so-called response functions) are also computed, as this information is needed by the fitting procedure. The synthetic B_I and r_0 are then compared to those actually measured by the SHABAR and S-DIMM. In general, the synthetic values will not match the measurements. The algorithm then uses the information in the response functions to calculate the first-order corrections $\delta C_n^2(h_i)$ that minimize the difference (in a least-squares sense) between the synthetic and measured values of $B_I(d)$ and $r_0(h = 0)$.
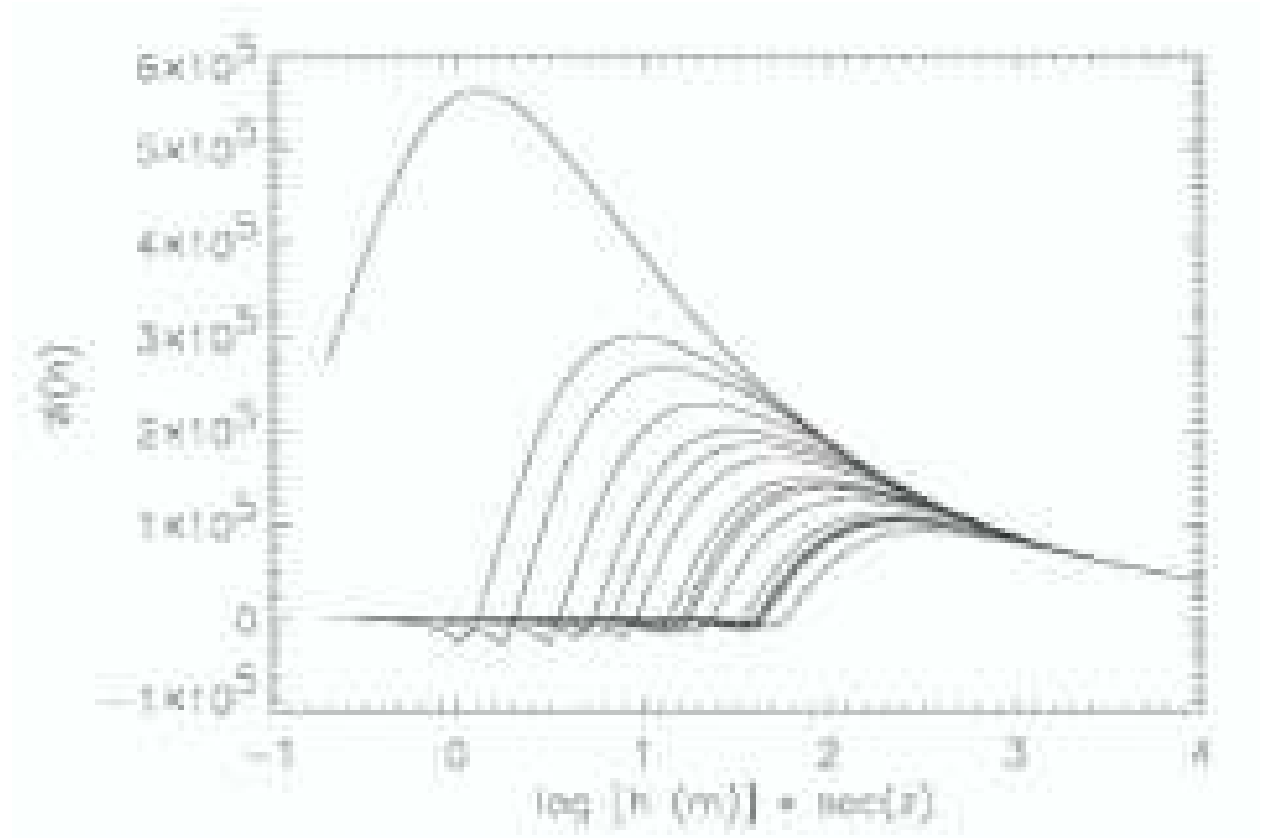
Fig. 1.— Height dependence of the inversion kernels $W(h, d)$ for the scintillation and the fifteen covariances (for various values of d) between brightness fluctuations measured by the SHABAR. The upper and lower curves correspond, respectively, to the smallest and largest sperations (0 and 468 mm). z is the solar zenith angle.
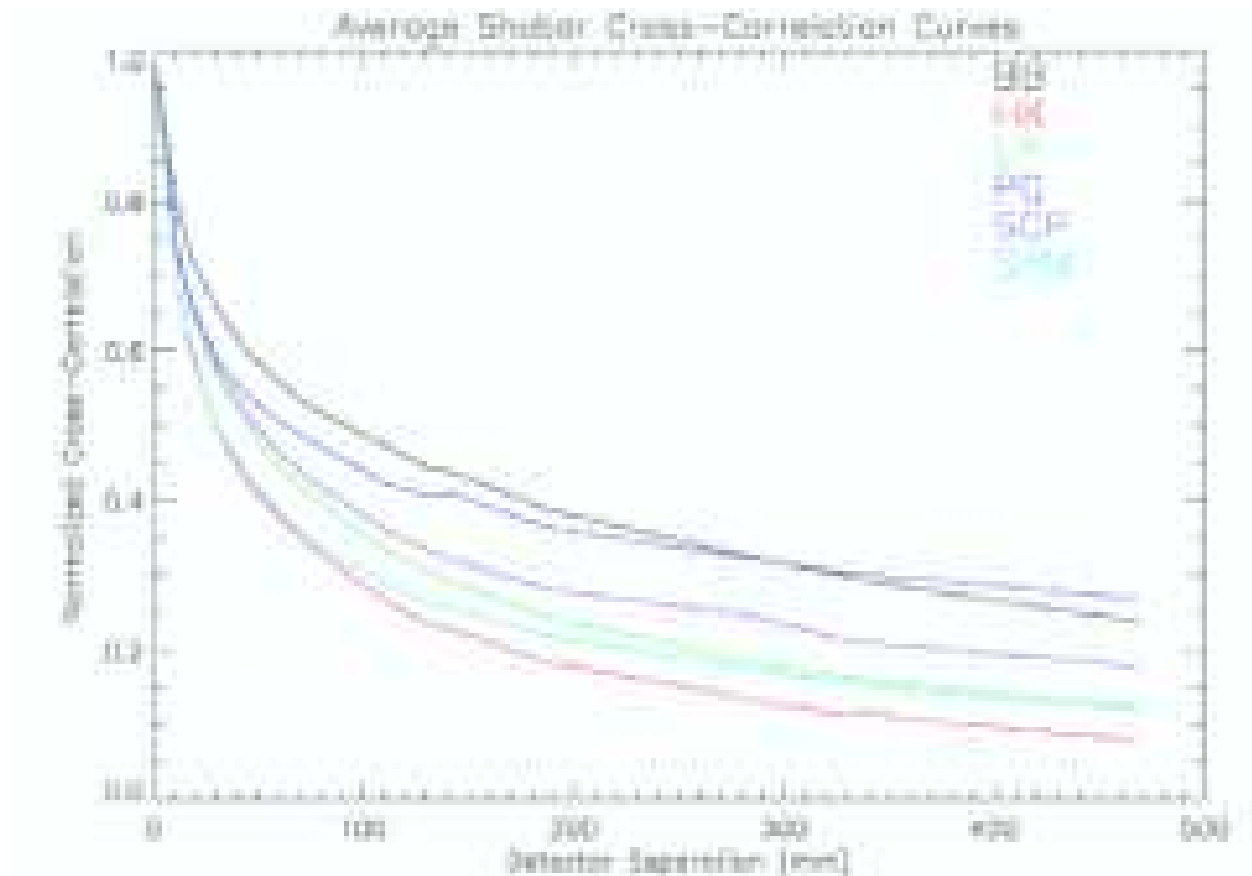
Fig. 2.— The average cross-correlation curves for the sites as of October 2003. The two lake sites, Big Bear (BB) and Panguitch (PG), have relatively shallow curves as a function of detector separation which indicates that the seeing arises from a region far above the instrument. The four non-lake sites have a relatively steeper cross-correlation as a function of separation, suggesting a boundary layer near the telescope.

The numerical solution of an inverse problem such as the one described here is always challenging, but even more is to ensure that the results obtained are physically meaningful. Understanding the issues and uncertainties involved in the inversion is critical for the success of the site survey and, ultimately, the ATST. It is equally important to ensure that the numerical codes employed are exhaustively tested and debugged. Based on previous experience with conceptually similar problems, the SSWG decided that two different codes should be independently developed and applied to the data. The two codes, based on the same minimization scheme described above, exhibit some differences in the actual implementation. By comparing the results provided by two different codes, we can learn about the reliability of the procedure and the limitations of our seeing measurements. Since there is no reason to prefer one above the other, we take the difference between their respective results as an estimate of the error bar.

2.2.1. The IAC code

The first code was developed at the Instituto de Astrofísica de Canarias (IAC) and run by National Solar Observatory (NSO) staff. The spatial grid is equispaced in $\log(h)$ with 68 points ranging from 20 cm to 40 km. However, not all of these points are inverted for (the problem would be ill-posed due to the large number of free parameters). Instead, $C_n^2(h)$ is determined at a subset of 17 special locations, the so-called inversion nodes. The rest of the atmosphere is then reconstructed via splines interpolation from the values at the nodes.

In order to ensure that $C_n^2(h)$ is always positive, we used the following change of variable. The code solves for a variable y such that $y(h) = \log[C_n^2(h)]$. In this manner, regardless of whether y is positive or negative, $C_n^2(h)$ will always be positive. Before inverting, the measured B_I and $r_0(h = 0)$ are processed with a 5-minute running median filter to smooth out fluctuations due to instrumental issues or problems such as birds or insects flying by the detectors.

After an initial application of the code to a sample dataset, it was found that a significant number of points could not be successfully fitted by the procedure. The observed $r_0(h = 0)$ provided by the S-DIMM instrument was inconsistent with the observed scintillation values $B_I(d)$ from the SHABAR. In all cases the S-DIMM r_0 was smaller than would be expected from the scintillation measurements. To overcome this difficulty we introduced an additional parameter Δs in the inversion that accounts for this "missing scintillation", so that the synthetic B_I are now given by:

$$B_I(d) + \Delta s = 0.38 \int_0^\infty W(h, d)C_n^2(h)dh \,, \tag{4}$$

while Eq (1) is still used to compute $r_0(h)$.

The necessity to include Δs points towards the existence of a a source of image degradation that does not produce scintillation. This may be due to a finite outer turbulence scale, to "windfiltering" (due to the finite time amount it takes for the turbulence to cross the field-of-view at high altitudes) or to high-altitude seeing (higher than ~ 1 km, where the kernels converge). In either case, the inclusion of Δs would be appropriate. While we have not been able to pinpoint the exact nature of the missing scintillation, the statistical distribution of Δs (see Fig 3) provides an interesting clue.

The two island sites (La Palma and Haleakala) require a relatively small amount of missing scintillation, whereas the lake site (Big Bear) frequently demands a substantially larger value. As we discuss below, the seeing in the island sites is typically dominated by a boundary layer near the ground and the turbulence decreases rapidly as we move upwards. The lake sites, on the other hand, are frequently dominated by high-altitude seeing. Thus, it seems likely that the Δs is related to the turbulence above the sensitivity range of the SHABAR.

2.2.2. The HAO code

The second inversion code was developed independently at the High Altitude Observatory (HAO). One of the essential differences with the IAC code is that all the grid-points in the atmospheric discretization are now free parameters. In order to make the algorithm stable, a regularization scheme was implemented in such a way that the code prefers smooth solutions whenever possible. Basically, in each iteration we add a penalization term to the χ^2. This term is proportional to the quadratic deviation of $C_n^2(h)$ from a straight line on a log-log plot. The fact that each grid-point is a free parameter represents an important burden that slows down the execution of the code. This is compensated, to some extent, by the more accurate integration scheme described below.

The model atmosphere only goes up to a maximum height $H_m = 1000/\sec(z)$ where the inversion kernels merge (Fig 1). We still consider the effect of turbulence above H_m by breaking down the integrals as:

$$B_I(d) = 0.38 \left(\int_0^{H_m} W(h,d)C_n^2(h)dh + B_I^{High} \right) \tag{5}$$

and

$$r_0^{-5/3}(h) = C\sec(z) \left(\int_h^{H_m} C_n^2(h)dh + \alpha B_I^{High} \right) . \tag{6}$$

Note that B_I^{High} does not depend on d. As before, α and B_I^{High} are free parameters that account for the scintillation and image degradation coming from high-altitude turbulence.

Another important difference with the IAC code is the integration scheme used to solve Eqs (5) and (6). The integral over each finite grid interval is computed assuming a parabolic dependence of $\log(C_n^2)$ with $\log(h)$ (see the appendix for details). While this integration introduces some additional complexity in the algorithm, it also alleviates the computational expense of the inversions by allowing a coarser grid without loss of accuracy.

The data pre-processing includes a 5-minute block average and a test to look for clouds in the averaged interval. If the derivative of the intensity measured by the SHABAR detectors changes sign two or more times, the entire period is flagged as cloudy and the $r_0(h)$ is set to zero at all heights.

3. Verification tests

3.1. Comparison of two codes

A sample subset of data (those taken in May 2003) were subject to inversion with both codes. Fig 4 shows the cumulative distributions produced by each code at La Palma, Haleakala and Big Bear. The results are fairly similar for most of the height range represented in the figure. As one would expect, the discrepancy increases with height due to the limited sensitivity of the SHABAR measurements to turbulence at higher layers. The same behavior is observed with the in situ measurements (see section 3.2 below).

A more detailed representation is given in Figs 5 and 6, which show the average stratifications of C_n^2 and r_0 with height. The C_n^2 produced by the HAO code has more spatial structure (small-scale fluctuations) than the IAC code. However, the overall dependence is actually very similar and the IAC results resemble a smoothed-out version of those from HAO (at least down to the first meter above the detectors). Whether the fine structure inferred by the HAO code is real or not is practically irrelevant for our purposes here, as the $r_0(h)$ parameter, which is our ultimate goal, is barely sensitive to it. The r_0 stratifications from both codes are very similar, at least up to ~ 40 m above the instrument. In this small sample we can already see the different behavior of the lake sites (Big Bear and Panguitch) as opposed to the island (La Palma and Haleakala) and continental sites (San Pedro Mártir and Sac Peak). The Big Bear plot exhibits a larger r_0 near the ground, but it does not improve significantly with height. The island and continental sites, on the other hand, have a lower value at the ground but the seeing improves dramatically as we go to higher layers, suggesting the presence of a boundary layer near the ground. The slope is particularly steep

in the $\sim$30-40 m range, precisely where the ATST aperture will be. These results emphasize the importance of analyzing the height dependence of r_0, as we have done in this work, since the site and height of the telescope may end up being critical factors in the performance of the ATST.

3.2. In situ measurements

Perhaps the most reliable test of the ATST site survey analysis is to compare its results directly with actual in situ measurements. The SSWG had access to a tower with meteorological instrumentation including hygrometers and sonic anemometers at various heights (DASH, Oncley & Horst 2004). With this instrumentation it is possible to make local measurements of temperature T and humidity q up to a height of $\sim$100 m. These parameters are monitored at a rate of 30 Hz, from which C_n^2 can be derived.

A complete SHABAR/S-DIMM system was deployed in Erie (Colorado), at the base of the measuring tower. Simultaneous measurements from the tower and the ATST instrumentation have been used to produce the scatter plots in Fig 7. Each panel shows the diagonal of the plot, as well as the Pearson correlation between the ATST inversions and the SHABAR instrumentation. Before analyzing the discrepancies between the two, a brief explanation is in order. While the tower measurements are strictly local, the SHABAR detectors receive solar light that has passed through a cone of Earth atmosphere. Thus, the ATST instrumentation is sensitive to a field of view that becomes larger for higher heights. For this reason, the C_n^2 measured in situ is expected to exhibit larger temporal fluctuations than that from the ATST instrumentation, which is a spatial average over the SHABAR field of view. This effect, which can be seen in Fig 8, increases the scatter especially in the higher layers. Moreover, the SHABAR field of view is displaced with respect to the tower instrumentation by an amount that increases with height. In any case, Fig 8 shows that the overall trends are in general well retrieved by the ATST analysis.

The tests indicate good agreement between both types of measurements up to a height between 22 and 50 m. It is important to note that the height range where the ATST measurements are accurate is lower in this case than at the actual candidate sites, simply because the tests were carried out during mid-winter at the considerably higher latitude of Erie (the $\sec[z]$ angle was always larger than 2.0).

While the Erie tests reassured our confidence in the ATST seeing measurements, there was still some concern that the atmospheric structure above the continental Colorado is probably very different from the actual sites. The SSWG then decided to mount similar

in-situ probes on a portable crane to perform similar tests on Big Bear and Haleakala. New measurements (this time considering lower heights due to the limitations of the crane) were conducted at the two sites, with the results shown in Fig 9.

The Haleakala tests show excellent agreement between the inversions and the measurements. In Big Bear, however, the correlation is very weak. Among the differences between the two sites are the level of humidity, the local topography and environment, and the probable lack of a ground boundary layer in Big Bear.

A possible explanation may be that the weaker scintillation in Big Bear makes these measurements more sensitive to noise. A closer look at the data shows that the correlation is improved by removing outlier points and clouds (Fig 10). Particularly interesting is the dataset gathered on May 12 2004, which reveals the dependence of the data with the wind direction (Fig 11). When the wind blows from the lake (west), the observing conditions are optimal and the seeing is dominated by high-altitude turbulence. On that particular day the wind changed from west to variable directions, resulting in the development of a ground turbulence layer and improving the correlation coefficient to ~ 0.77. Note also that, in the absence of a surface turbulence layer at Big Bear, r_0 will essentially be independent of h near the ground and the S-DIMM measurements at 8 m can be taken to represent r_0 at 25-40 m.

4. Conclusions

The ATST project has imposed stringent requirements on the telescope site, both in terms of seeing and sky brightness. The seeing analysis has proven very challenging due to the strong dependence of r_0 with height exhibited by most sites. This paper describes the analysis employed by the ATST SSWG to find the site that provides optimal conditions (r_0) at the height of the ATST primary aperture.

Various tests have been used to demonstrate the validity of our analysis, at least up to ~ 40 m above the ground. The use of two independent inversion codes are helpful to understand the uncertainties in the procedure and to set error bars on the measurements. Moreover, in situ measurements proved the validity of the approach in the height range of interest. The only caveat identified by our work is that the errors increase when the seeing is dominated by high-altitude turbulence (i.e., in the absence of a ground boundary layer).

A. Parabolic integration scheme

Let $x = \log(h)$ and $y = \log[C_n^2(h)]$. If we approximate y and W as parabolic functions of x:

$$W = w_1 x^2 + w_2 x + w_3 \tag{A1}$$
$$y = ax^2 + bx + c,$$

we can solve analytically the integral in Eq (5) between two adjacent grid-points x_1 and x_2, as:

$$
\begin{aligned}
I &= \int_{x_1}^{x_2} \left[w_1 x^2 + w_2 x + w_3 \right] 10^{\left(ax^2 + bx + c \right)} dx \tag{A2} \\
&= 10^c \int_{x_1}^{x_2} \left[w_1 x^2 + w_2 x + w_3 \right] 10^{\left(ax^2 + bx \right)} dx \\
&= 10^c \left(T_1 + T_2 + T_3 \right)
\end{aligned}
$$

where,

$$
\begin{aligned}
T_1 &= \frac{2^{-3-\frac{b^2}{4a}} w_1}{5^{\frac{b^2}{4a}} a^{\frac{5}{2}} \log(10)^{\frac{3}{2}}} \left\{ 2^{1+\frac{b^2}{4a}} 5^{\frac{b^2}{4a}} \sqrt{a} \left(\left(10^{x_1 (b+a x_1)} - 10^{x_2 (b+a x_2)} \right) b \right. \right. \\
&\quad + 2a \left(-\left(10^{x_1 (b+a x_1)} x_1 \right) + 10^{x_2 (b+a x_2)} x_2 \right) \left. \right) \sqrt{\log(10)} \\
&\quad + \sqrt{\pi}\, \mathrm{Erf}\!\left(\frac{(b+2a x_1) \sqrt{\log(10)}}{2\sqrt{a}} \right) \left(2a - b^2 \log(10) \right) \\
&\quad + \sqrt{\pi}\, \mathrm{Erf}\!\left(\frac{(b+2a x_2) \sqrt{\log(10)}}{2\sqrt{a}} \right) \left(-2a + b^2 \log(10) \right) \left. \right\}
\end{aligned}
$$

$$
\begin{aligned}
T_2 &= \frac{2^{-2-\frac{b^2}{4a}} w_2}{5^{\frac{b^2}{4a}} a^{\frac{3}{2}} \log(10)} \left\{ 2^{1+\frac{b^2}{4a}} 5^{\frac{b^2}{4a}} \left(-10^{x_1 (b+a x_1)} + 10^{x_2 (b+a x_2)} \right) \sqrt{a} \right. \\
&\quad + b\, \mathrm{Erf}\!\left(\frac{(b+2a x_1) \sqrt{\log(10)}}{2\sqrt{a}} \right) \sqrt{\pi\, \log(10)} \\
&\quad - b\, \mathrm{Erf}\!\left(\frac{(b+2a x_2) \sqrt{\log(10)}}{2\sqrt{a}} \right) \sqrt{\pi\, \log(10)} \left. \right\}
\end{aligned}
$$

$$
\begin{aligned}
T_3 &= -\frac{2^{-1-\frac{b^2}{4a}} w_3}{5^{\frac{b^2}{4a}} \sqrt{a}} \left(\sqrt{\frac{\pi}{\log(10)}} \right) \left\{ \mathrm{Erf}\!\left(\frac{(b+2a x_1) \sqrt{\log(10)}}{2\sqrt{a}} \right) \right. \\
&\quad - \mathrm{Erf}\!\left(\frac{(b+2a x_2) \sqrt{\log(10)}}{2\sqrt{a}} \right) \left. \right\}
\end{aligned}
$$

REFERENCES

Beckers, J. M. 2001, Experimental Astronomy, 12, 1

Brandt, P. N., & Righini, A. 1985, Vistas in Astronomy, 28, 437

Brandt, P. N., & Woehl, H. 1982, A&A, 109, 77

Hickson, P., & Lanzetta, K. 2004, PASP, 116, 1143

Keil, S. L., Rimmele, T., Keller, C. U., Hill, F., Radick, R. R., Oschmann, J. M., Warner, M., Dalrymple, N. E., Briggs, J., Hegwer, S. L., & Ren, D. 2003, in Innovative Telescopes and Instrumentation for Solar Astrophysics. Edited by Stephen L. Keil, Sergey V. Avakyan . Proceedings of the SPIE, Volume 4853, pp. 240-251 (2003)., 240–251

Oncley, S., & Horst, T. 2004, Calculation of C_n^2 for visible light and sound from CSAT3 sonic anemometer measurements, available at http://www.atd.ucar.edu/homes/oncley/bao2004/background.pdf

Press, W. H., Flannery, B. P., & Teukolsky, S. A. 1986, Numerical recipes. The art of scientific computing (Cambridge: University Press, 1986)

Zirin, H., & Mosher, J. M. 1988, Solar Phys., 115, 183
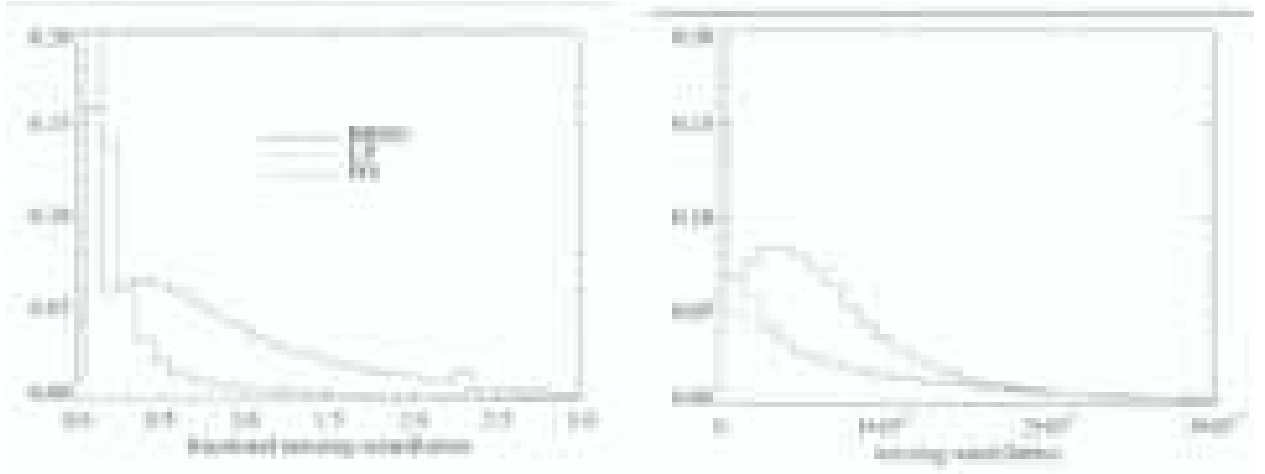
Fig. 3.— Histograms of the relative frequency of occurrence of missing scintillation Δs values at the three sites. Left: relative occurrence of Δs as a fraction of the observed scintillation; left: entire distribution; Right: relative occurrence of Δs as an absolute scintillation measure. Solid line: Big Bear; Dashed line: Haleakala; Dotted line: La Palma. Note that the two mountain sites (La Palma and Haleakala) typically require 10-20% fractional Δs while the lake site (Big Bear) frequently needs a substantially larger value.
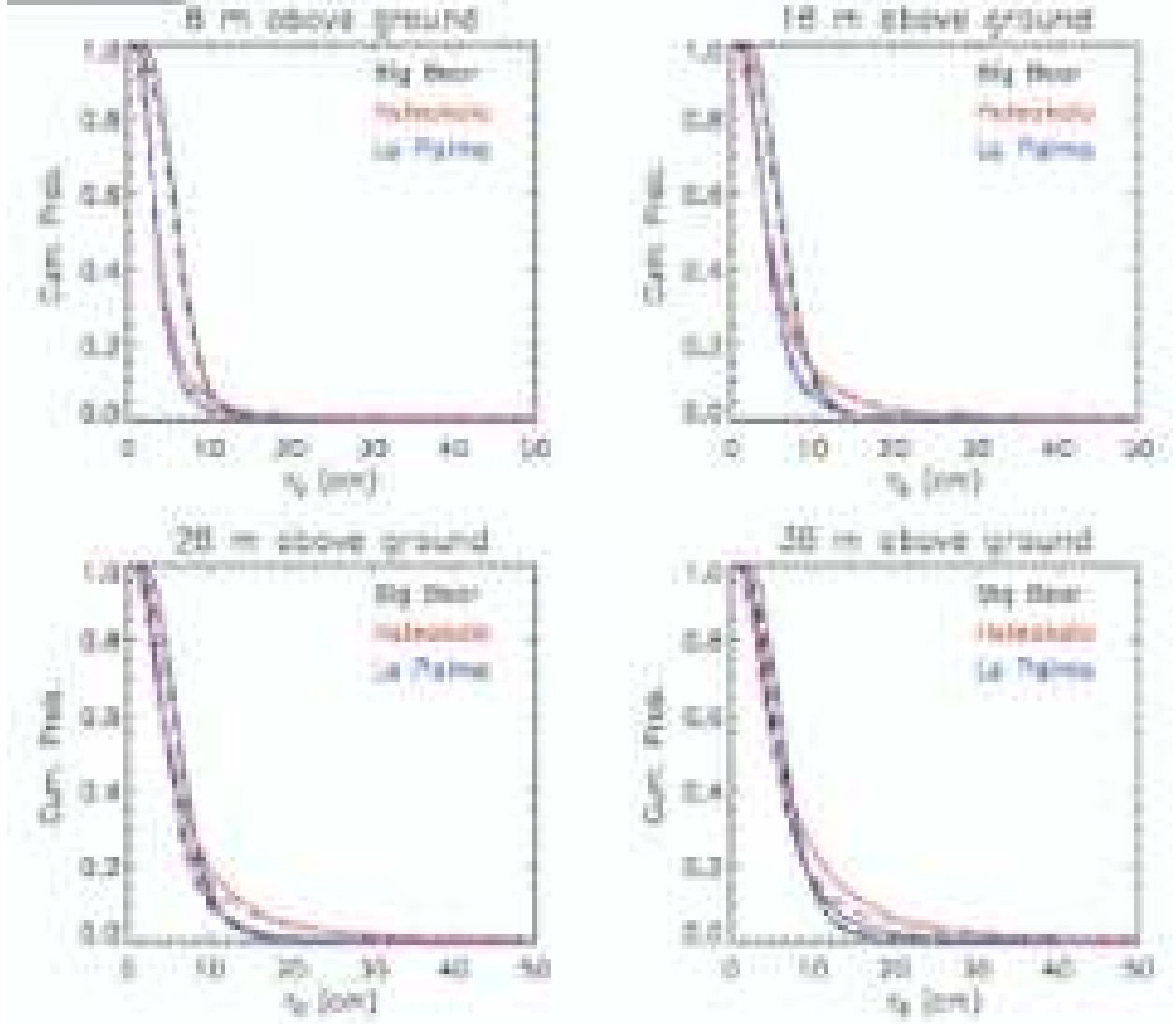
Fig. 4.— A comparison between the two inversion methods. Here we show the cumulative distribution of the esimated $r_0(h)$ at the three sites and at four heights, as derived from the HAO method (dashed line) and the IAC method (solid line).
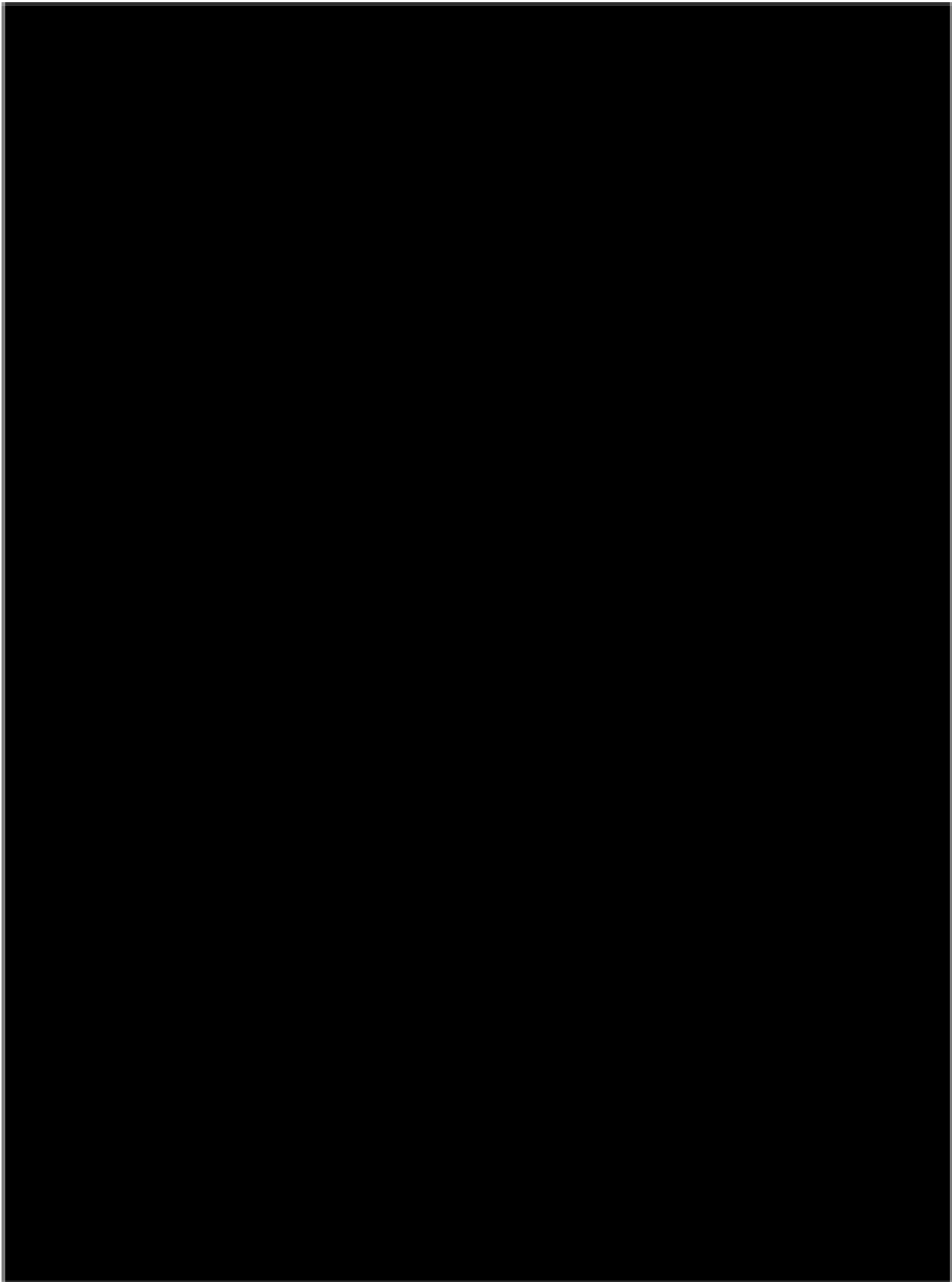
Fig. 5.— Curves of $C_n^2(h)$ and $r_0(h)$ retrieved by the inversions averaged over May 2003 for Big Bear, Haleakala and La Palma. Dashed: HAO method, Solid: IAC method.
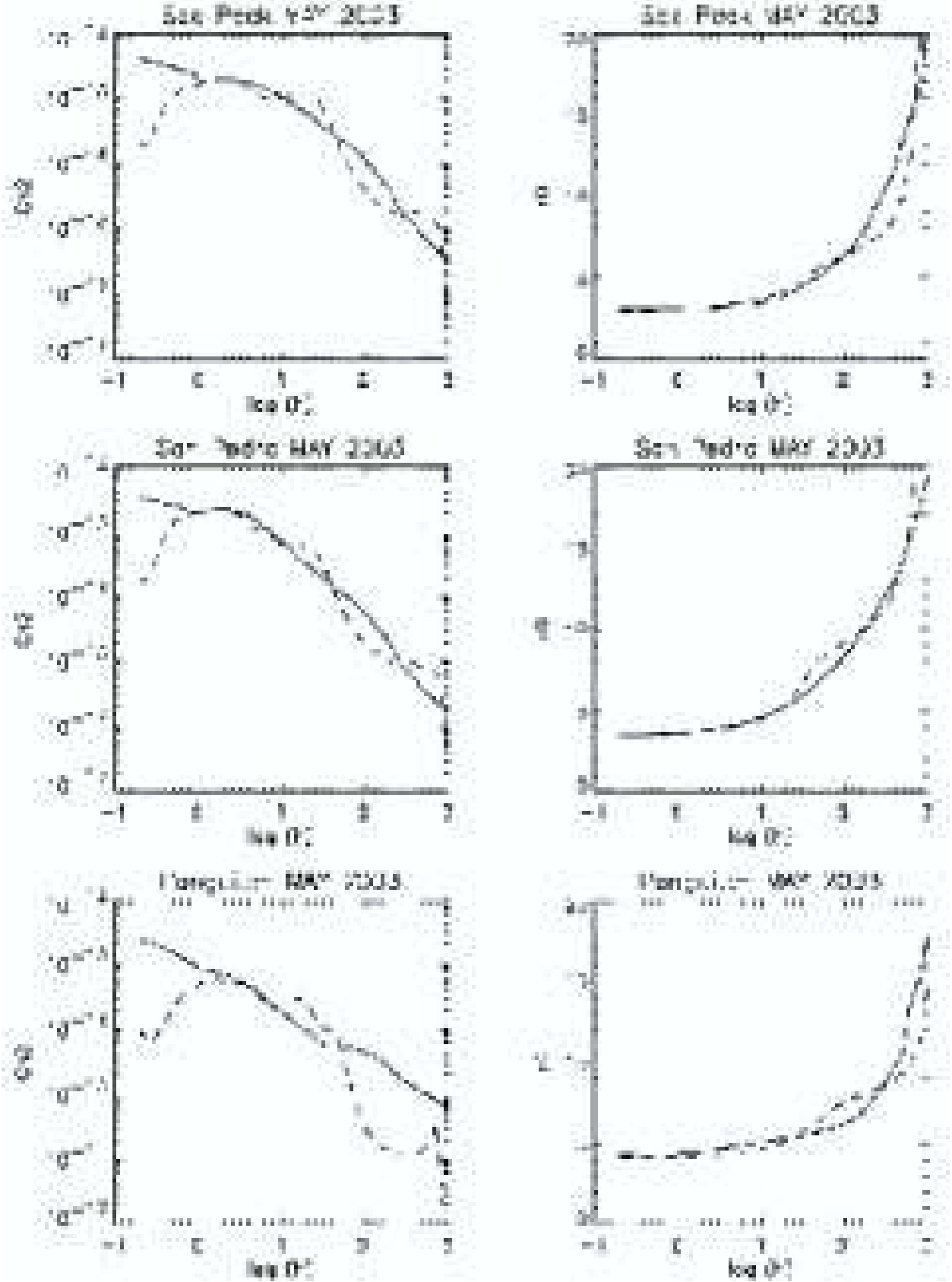
Fig. 6.— Curves of $C_n^2(h)$ and $r_0(h)$ retrieved by the inversions averaged over May 2003 for Sac Peak, San Pedro Mártir and Panguitch. Dashed: HAO method, Solid: IAC method.
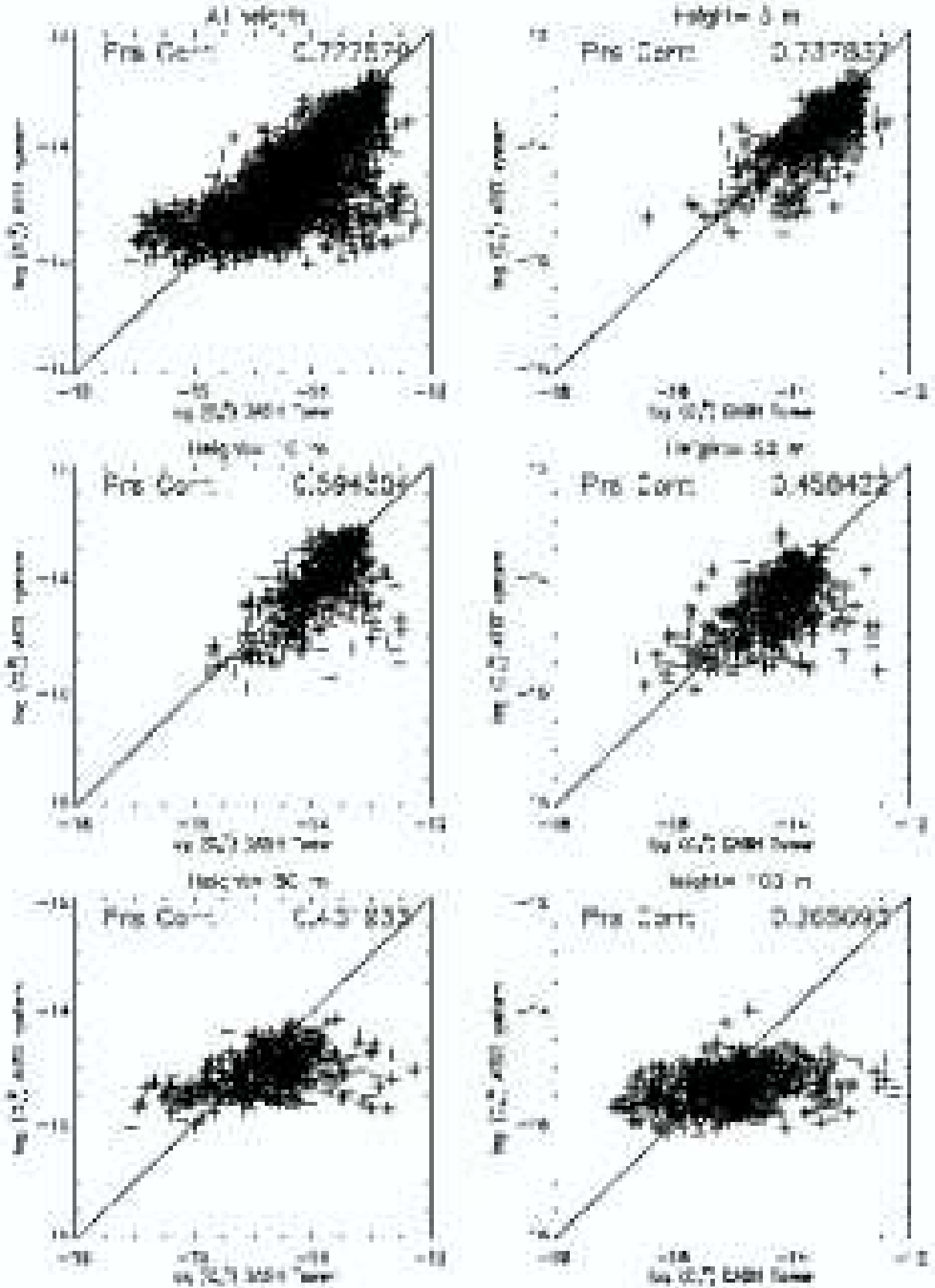
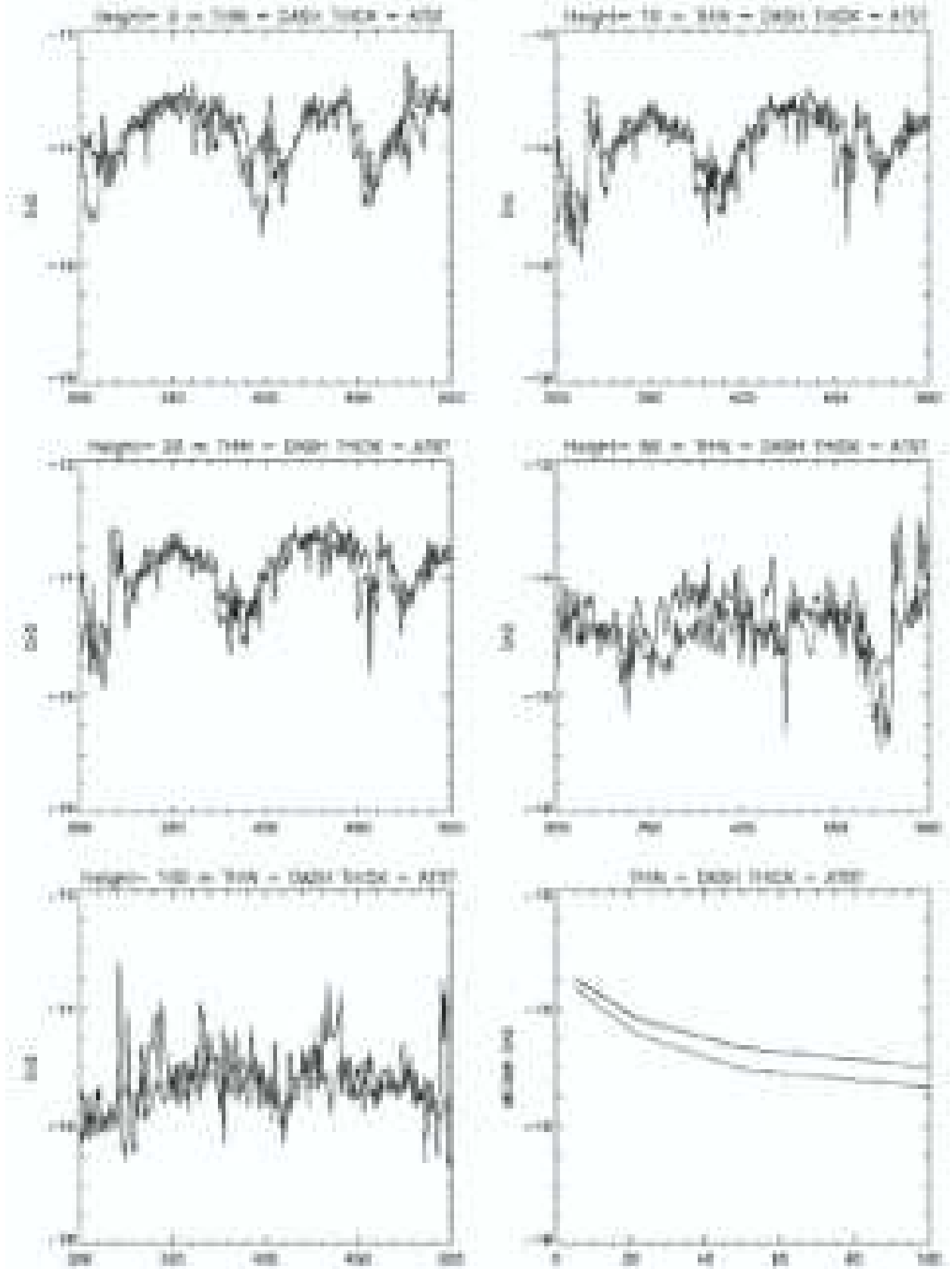Fig. 7.— Comparison of C_n^2 from the ATST system with in situ measurements in Erie, Colorado.

Fig. 8.— Time series determinations of C_n^2 with the Erie tower and the ATST instrumentation at 5, 10, 22, 50 and 100 m. Bottom-right panel: Median value as a function of height.
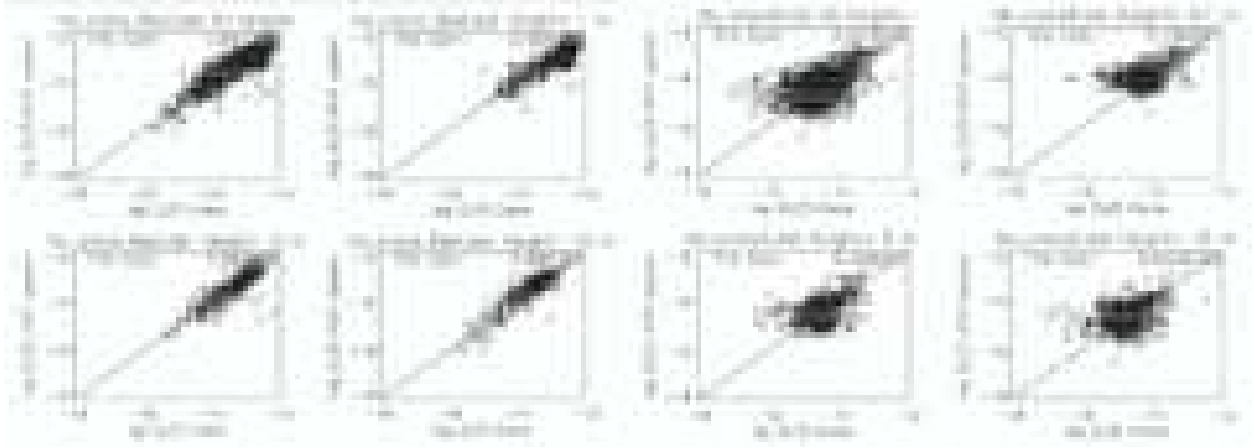
Fig. 9.— Scatter plot comparisons between the ATST estimates and the in situ measurements of C_n^2 at Haleakala (left four panels) and Big Bear (right four panels). In each four-panel set the comparison is for the three heights of the in situ measurements, plus all of the points combined. The straight line is strict equality, and each plot is labeled with the Pearson correlation coefficient of the data.
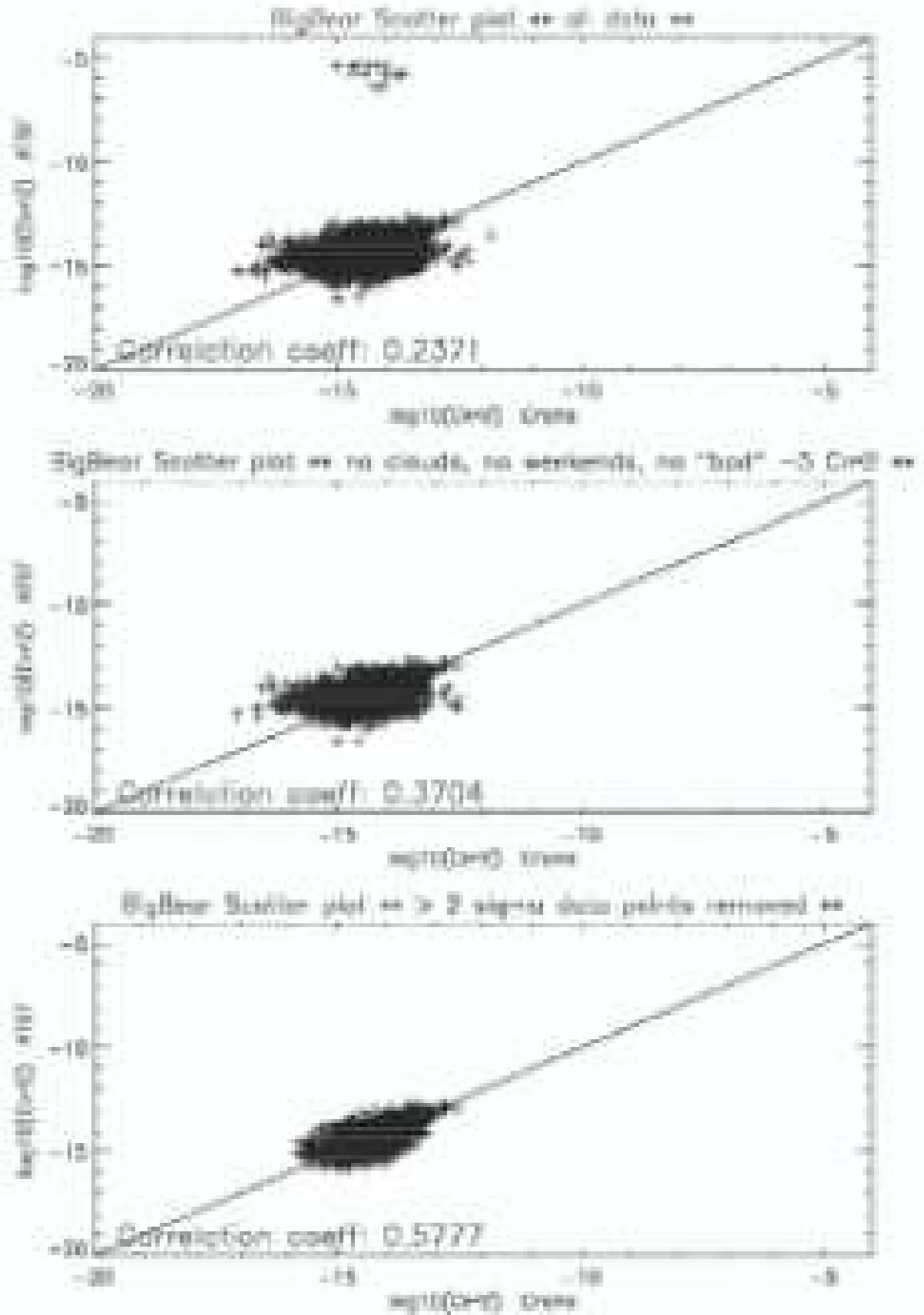
Fig. 10.— The influence of noise on the correlation between the ATST and in situ measure-
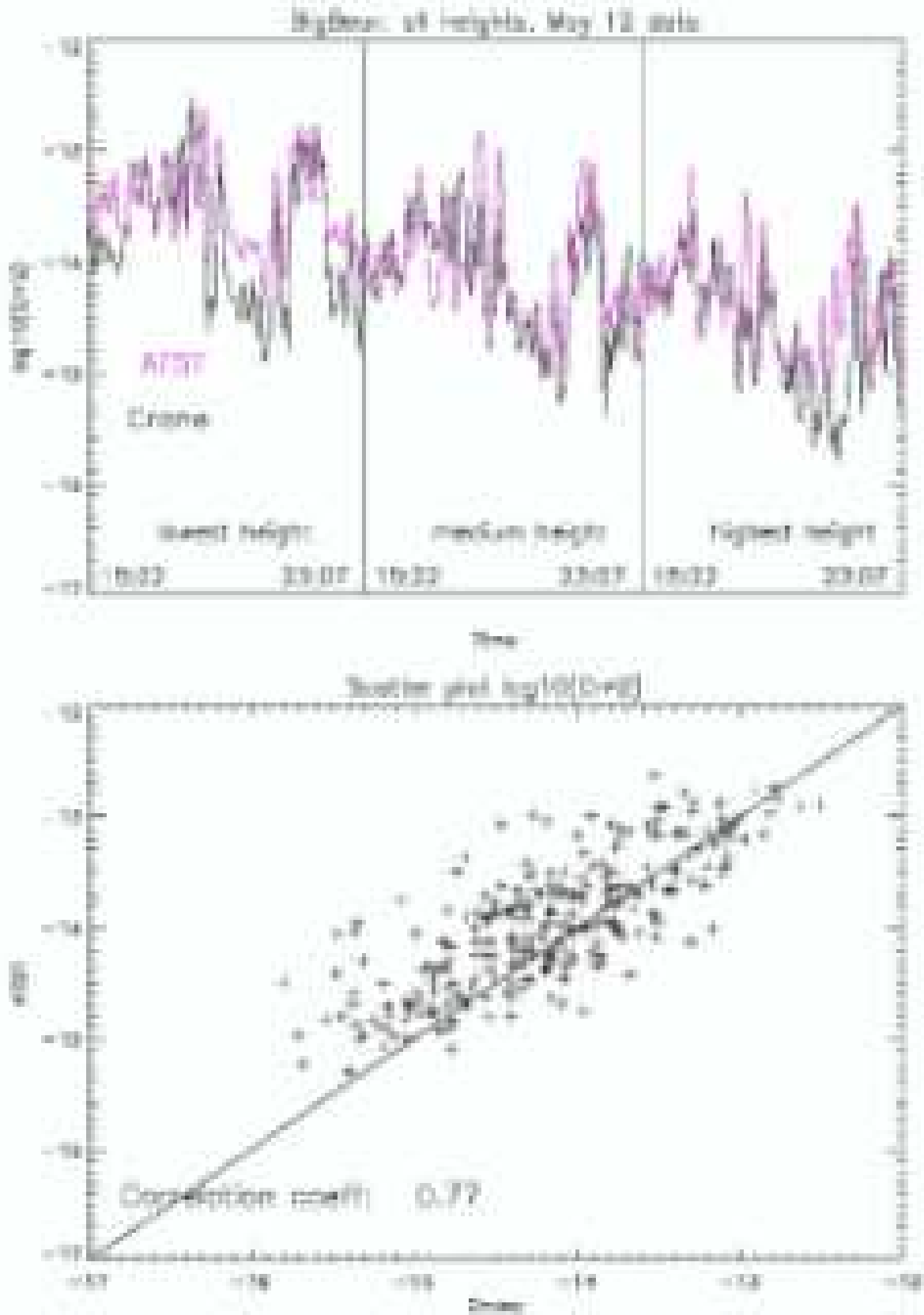
Fig. 11.— The correlations for Big Bear on May 12, 2004 when the winds were atypically variable. Top: time series for the three heights. Bottom: correlation for this day.